

## Flux quantization in weak links in melt-textured bulk $\text{YBa}_2\text{Cu}_3\text{O}_{7-x}$

J. Wosik, L. M. Xie, and J. C. Wolfe

*Texas Center for Superconductivity at University of Houston and Electrical Engineering Department,  
University of Houston, Houston, Texas 77204*

Y. Ren and C. W. Chu

*Texas Center for Superconductivity at University of Houston and Physics Department, University of Houston, Houston, Texas 77204*

(Received 21 June 1994; revised manuscript received 16 January 1995)

We have studied flux quantization in weak links of  $a$ - $b$ - and  $a$ ( $b$ )- $c$ -plane-oriented, melt-textured  $\text{YBa}_2\text{Cu}_3\text{O}_{7-x}$  using a modulated-field microwave-absorption method. First derivative of the microwave absorption versus dc magnetic field was measured in a  $\text{TE}_{102}$  cavity at 9.5 GHz. We observed several series of well-resolved equally spaced absorption lines in the externally applied dc magnetic field with separation ranging from 6  $\mu\text{T}$  to 2.3 mT. By analyzing the dependence of these series on microwave power, temperature, and orientation of the sample versus dc magnetic field we have identified the types and locations of Josephson-junction weak links in the samples. One of the series was found to be related to the microwave absorption in a strongly coupled superconductor-normal-metal-superconductor type of junction located in intragrain plane defects (complex twin boundaries). For this junction, the critical current  $I_c$  dependence on magnetic field  $B$  as well as lower critical field  $B_{c1J}$  were determined. For the location of the inter- and intragrain plane defects we have found  $C_2$  and  $C_4$  symmetry, respectively. A physical model of microwave absorption in nonuniform Josephson junctions is presented and sample microstructure is correlated with the measurement results.

### I. INTRODUCTION

The understanding of microwave absorption in high- $T_c$  superconductors is far from complete, in spite of an increasing number of papers on microwave properties of high- $T_c$  superconductors (HTS's). Though there are many intensive studies of grain boundaries in  $\text{YBa}_2\text{Cu}_3\text{O}_{7-x}$  (YBCO), several problems crucial to the understanding of transport properties remain unsolved. One of the most important questions refers to the type of junctions present in the material and their location, which is especially important for tape and wire applications. Microwave experiments can be, in general, divided into two types: (a) measurements of the effective surface impedance of a superconductor with an without dc magnetic field using microwave resonators,<sup>1-3</sup> and (b) measurements of microwave absorption versus dc magnetic field using magnetic-field modulation for high sensitivity. In the latter case commercial electron spin resonance (ESR) spectrometers<sup>4,5</sup> are often used. ESR spectrometers are typically designed to measure very small changes in the microwave absorption during a slow scan of the dc magnetic field for investigation of electron-spin-resonance phenomena. To enhance the signal-to-noise ratio, a phase-sensitive detection system is used which requires implementation of an ac magnetic-field modulation in addition to dc magnetic field ( $B_{dc}$ ). This results in three simultaneous magnetic fields: the microwave magnetic field ( $B_{rf}$ ), scanning dc field, and ac modulation field; the  $B_{dc}$  and  $B_{rf}$  fields are mutually perpendicular. This technique, because of its exceptional sensitivity, has been used successfully in the study of high- $T_c$  superconductivity to measure quantitatively the modulated-field microwave

absorption (MFMA) at low magnetic field<sup>6</sup> as well as magnetic-flux quantization in weak links of HTS materials.<sup>7</sup>

MFMA in polycrystalline samples at low magnetic fields shows broad absorption with hysteretic behavior and sometimes reproducible noiselike fluctuations with a periodic structure.<sup>8</sup> However, measurements in single crystals show a series of very well-resolved, equally spaced absorption lines which are not observed in surface impedance measurements and which are related to the Josephson weak links. A series of such lines were reported by Blazey *et al.*<sup>9</sup> and were attributed to the presence of twin boundaries in single crystals. The presence of such an electromagnetic response is not a unique feature of high- $T_c$  superconductors because similar series of uniformly spaced lines were reported later in niobium,<sup>10</sup> indium,<sup>11</sup> and in the lead Chevrel-phase compound  $\text{PbMo}_6\text{S}_8$ .<sup>12</sup> Drumheller, Trybula, and Stankowski<sup>13</sup> reported these kinds of spectra in two pieces of lead which were pressed together. While it is generally agreed that the origin of the lines is related to the flux quantization in planar defects in crystals, it is not clear if the spacing between these lines is determined by the area of a hypothetical superconducting ring with one or more Josephson weak links intercepting the magnetic flux  $\Phi$  or by the area of a single Josephson-junction defect.

In the present work we report the results of an experimental and phenomenological study of microwave absorption of weak links in melt-textured bulk samples using the MFMA method. The investigation was designed to provide some clarification on the relationship between the defects in superconductive materials and flux quantization obtained from experimental data. This informa-

tion is important not only for the investigation of the origin of microwave losses in these materials but also for understanding of  $J_c$  limitation due to the presence of weak links and of the role of point and planar defects as pinning centers. To realize this program we have chosen a melt-textured material. From measurements of surface resistance in a dc magnetic field, it is well known that below 0.1 T microwave losses in this material are governed by Josephson weak links. In addition, this material contains large grains with very good crystallographic quality as well as well-defined and structured inter- and intragrain boundaries.<sup>14</sup>

A number of theoretical models have been proposed to explain the periodic line series observed in single-crystal samples.<sup>15</sup> Most of the models follow the Silver and Zimmerman<sup>16</sup> theory of magnetic-flux quantization in superconducting loops containing at least one Josephson junction. In this paper we present another model which takes into account the orthogonal configuration of the  $B_{rf}$  and  $B_{dc}$  fields which is specific to the ESR spectrometer design. Such an approach is different from the Silver and Zimmerman theory where the two magnetic fields are parallel. Our approach is based on an analysis of microwave absorption in a single nonuniformly coupled junction using a nonlinear resistively shunted junction (RSJ) model.

## II. EXPERIMENTAL PROCEDURE

The microwave measurements were carried out using a conventional Bruker ESP 300 spectrometer operating at 9.5 GHz. An Oxford Instruments continuous-flow helium cryostat was used to obtain temperatures ranging from 4.2 to 300 K. The static magnetic field  $B_{dc}$  was horizontally aligned, while the microwave field was always perpendicular to the dc field. The estimated maximum available value of the rf magnetic field, related to the maximum incident power, was about 1 mT. The dc magnetic field was modulated at 100 kHz. Some measurements, where modulation frequency can influence the linewidth, were done using lower modulation frequency. In most of the measurements we used a very small modulation amplitude with a peak-to-peak value below 1  $\mu$ T. In the whole range of the magnetic-field modulation, the amplitude of the observed lines was a linear function of the modulation amplitude. We verified that the modulation had no influence on the periodicity of the line series. The shape of the lines depends on the origin of the microwave absorption and will be discussed later.

The samples were fabricated according to the procedure reported by Salama *et al.*<sup>17</sup> and were cut into  $1 \times 2 \times 0.3$  mm<sup>3</sup> platelets with the large faces parallel to the  $a$ - $b$  plane. Each sample was mounted on a Suprasil quartz rod and was placed in the center of the cavity. The samples were rotated with respect to the direction of the  $B_{dc}$  magnetic field using a single-axis goniometer. Two configurations have been studied: (i) rotation along the  $c$  axis of the sample and (ii) rotation along the  $a$  or  $b$  axis. The samples were heavily twinned and hence the  $a$  and  $b$  axes were indistinguishable. The four-quadrant type of magnet power supply allowed continuous scanning of  $B_{dc}$

from negative to positive values and zero-field cooling (ZFC). Most of the measurements were carried out with a very low microwave power, where the microwave current crossing junctions was used as a probe current and the flux quantization was due to the presence of the dc magnetic field. This subject is discussed in detail in Sec. V. Measurements of surface resistance versus temperature for these samples showed the superconductivity onset temperature of about 94 K with a relatively narrow transition.<sup>18</sup>

## III. RESULTS

We have observed numerous series of very well-resolved absorption lines for various sample orientations with respect to the dc magnetic field and to the incident microwave power. We have selected, for this investigation, only the series for which minima of the angular dependence of the line spacing ( $\Delta B$ ) could be related to the characteristic crystallographic directions in the samples. Figure 1 shows the three main types of line series selected for analysis. The first type of selected spectra have a short series of only a few lines [Fig. 1(a)]. The three first lines from this series are marked in Fig. 1(a) by single arrows. The second type is a series of equally

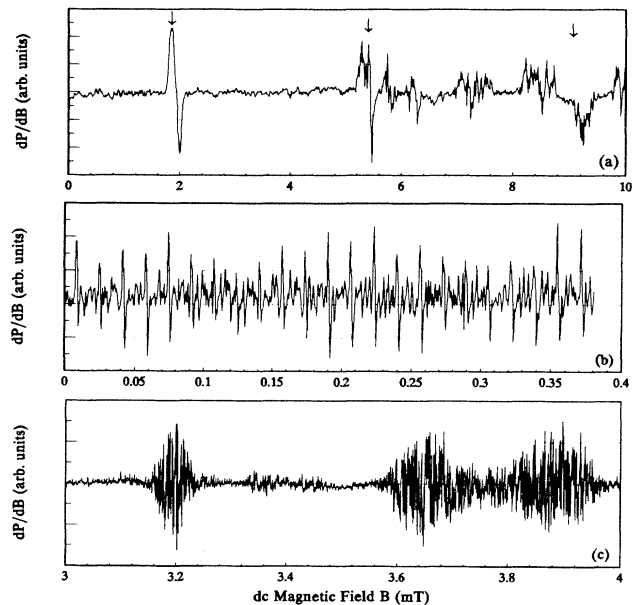


FIG. 1. Three main types of line series selected for analysis in this paper. (a) A short line series with large line spacing. The arrows mark the positions of the first three lines. Measurements were done at 32  $\mu$ W and 5 K. The experimental configuration is shown in the inset of Fig. 2 below. The angle between  $B_{dc}$  and the [110] direction was 50°. (b) A long line series with the line spacing two orders of magnitude smaller than for type 1. Measurements were done in the experimental configuration shown in the inset of Fig. 3 below (80  $\mu$ W and 5 K). The angle between  $B_{dc}$  and the  $a$  ( $b$ ) axis was 0°. (c) A modulated-amplitude line series with the line spacing of the order of  $\mu$ T. The experimental configuration was the same as for the case (b) but measurements were done at 2 mW.

spaced lines of the same amplitude; these lines can be observed in magnetic fields up to several mT [Fig. 1(b)]. The spacing between the lines is 0.016 mT, which is two orders of magnitude smaller than for the first type. The third type of spectra, observed only at higher microwave power than needed for the previous two types, has a modulated amplitude [Fig. 1(c)].

Different values of the threshold power are observed for each type of line series. The first and second types of line series showed thresholds of the order of  $\mu\text{W}$ , whereas for the third type input power was of the order of mW. Additionally, the first type of absorption line series has different power thresholds for the first and next lines. The first line appears at higher power level than is needed for the next lines to occur. The second and third type exhibit the same power threshold for the whole series.

The samples were zero-field cooled to 6 K and then exposed to a scan of the dc magnetic field. In the experiments, none of the recorded line series showed hysteresis and the relative amplitudes of the lines as well as their positions were unaffected by the scan time. The spacing between the lines of each type showed a strong angular dependence, as shown in Fig. 2 for the first series. The sample was rotated around the  $c$  axis; the experimental configuration shown in the inset was used. The external dc magnetic field was parallel to the  $a$ - $b$  plane and the  $B_{\text{rf}}$  field was parallel to the  $c$  axis. We observed the presence of two sets of lines, with angular dependencies of  $\Delta B$  shifted by  $90^\circ$ . The minima of the dependencies of  $\Delta B$  on  $\Theta$  were found for  $\Theta=0^\circ$  and  $\Theta=90^\circ$ , corresponding to  $B_{\text{dc}}$  parallel to the  $[110]$  and  $[\bar{1}\bar{1}0]$  directions, respectively. Both sets of lines can be associated with the same type of plane defects. Thus the  $C_4$  symmetry of the plane

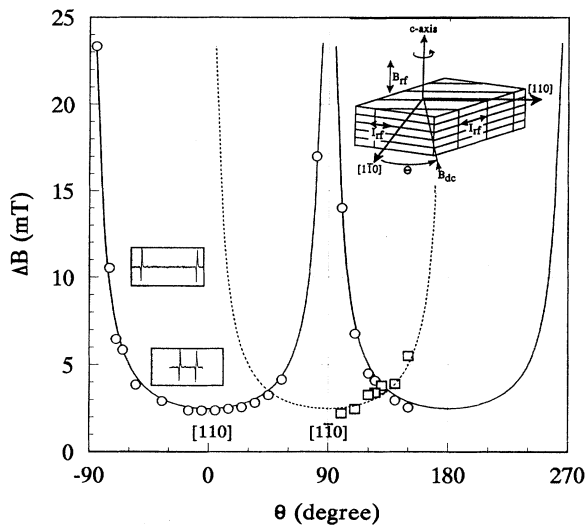


FIG. 2. Angular dependence of the periodic spacing between line series for the sample rotated around the  $c$  axis. The upper inset shows the experimental configuration during measurements. Minimum of  $\Delta B$  ( $\Theta=90^\circ$ ) corresponds to  $B_{\text{dc}}$  parallel to the  $[110]$  direction. The solid and dashed lines represent  $1/\cos\Theta$  fitting. Two other insets present the series of lines at  $\Theta=-70^\circ$  and  $0^\circ$ , having the periodic spacing  $\Delta B$  equal to 10.2 and 2.3 mT, respectively.

defects is identified for the  $a$ - $b$  plane of the sample. Two additional insets show the line series at two different angles  $\Theta$ . The scale of both insets is the same and the dc field scan is from  $-5$  to  $5$  mT.

The angular dependence of the line spacing for the second type of series is shown in Fig. 3. The inset shows the experimental configuration with the  $a$  ( $b$ ) axis used as the rotation axis, thus setting the  $c$  axis perpendicular to the rotation axis. In this arrangement the  $B_{\text{rf}}$  and  $B_{\text{dc}}$  fields are parallel and perpendicular to the rotation axis, respectively. This case is different from the angular dependence of  $\Delta B$  shown in Fig. 2 since only  $C_2$  symmetry of the plane defects is observed. It is deduced from the  $180^\circ$  periodicity of the spacing minima. These minima were found for  $\varphi=0^\circ$  and  $180^\circ$ , which correspond to  $B_{\text{dc}}$  parallel to the  $a$  ( $b$ ) axis. Two additional insets drawn in the same scale ( $0$ – $0.4$  mT) show the  $\Delta B$  spacing of the recorded spectrum for two different angles  $\varphi$ .

The spacing between the lines is  $\Delta B = \Phi_0/S$ , where  $\Phi_0 = h/2e$  is the flux quantum and  $S$  is the magnetic cross-sectional area for interception of the flux.  $S$  for a barrier of thickness  $d$  and length  $L$  is approximately equal to  $L(2\lambda + d)$ , since the field enters the grains to a distance determined by the superconducting penetration depth  $\lambda$ . The only effective field component is the one perpendicular to the cross-sectional area  $S$ , so the measured  $\Delta B$  will scale as  $\Delta B = \Delta B_0/\cos\Theta$ , where  $\Delta B_0$  is the spacing for  $\Theta=0^\circ$ , while  $\Theta$  is the angle between the field and unit vector normal to  $S$ . The solid and dotted lines shown in Fig. 2 represent  $1/\cos\Theta$  fitting and the solid line shown in Fig. 3 represents  $1/\cos\varphi$  fitting.

Since the cross-sectional area  $S$  intercepting the flux depends on the penetration depth, a study of the temper-

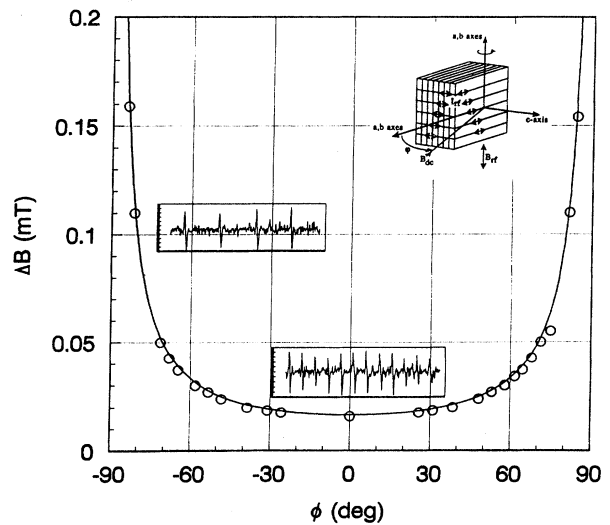


FIG. 3. Angular dependence of the periodic spacing  $\Delta B$  between the lines when the sample was rotated around the  $a$  ( $b$ ) axis. The upper inset shows the experimental configuration of the measurements.  $\varphi=0^\circ$  (minimum of  $\Delta B$ ) corresponds to  $B_{\text{dc}}$  parallel to the  $b$  ( $a$ ) axis. The solid line represents  $1/\cos\varphi$  fitting. Two other insets present lines series at  $\varphi=0^\circ$  and  $-70^\circ$ , showing the periodic spacing  $\Delta B$  equal to 0.016 and 0.045 mT, respectively.

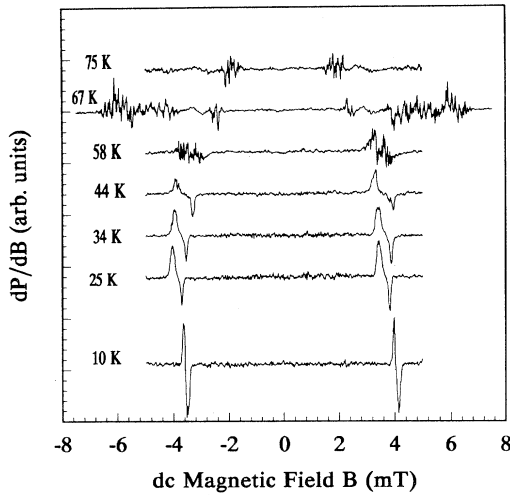


FIG. 4. Temperature dependence of the shape and line spacing in the range 10–75 K. The sample was measured in the configuration shown in the inset of Fig. 2. The angle between the [110] direction and the dc magnetic field was  $50^\circ$ .

ature behavior of  $\Delta B$  can give important information about the size and type of junctions. In order to test the temperature dependence of the shape and position of the first type of lines we measured the microwave absorption as a function of temperature. Figure 4 shows two lines of the first type of series recorded at different temperatures ranging from 10 to 75 K using constant microwave power. It was measured at  $\Theta=50^\circ$ ; thus  $\Delta B$  is 7.8 mT (see Fig. 2). This line spacing has the minimum value of 2.3 mT.

An increase of the microwave power has a different effect on each of the three types of spectra presented earlier in Fig. 1. The lines of the first type of spectrum measured at several different levels of microwave power are shown in Fig. 5. There is clear evidence of a power threshold for the first line in the series which appears

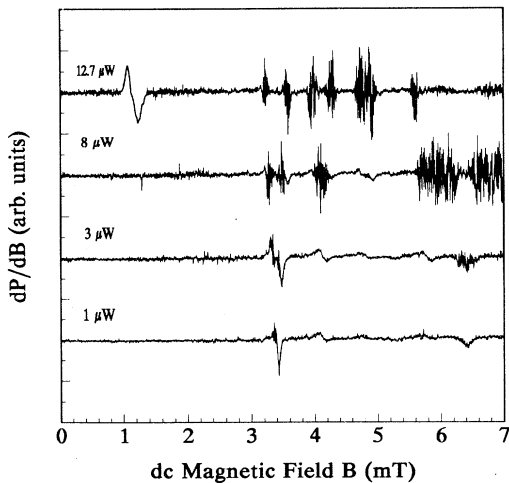


FIG. 5. Evidence for the power threshold for the first line from the first type of line series. The sample was measured using the experimental configuration shown in the inset of Fig. 2.

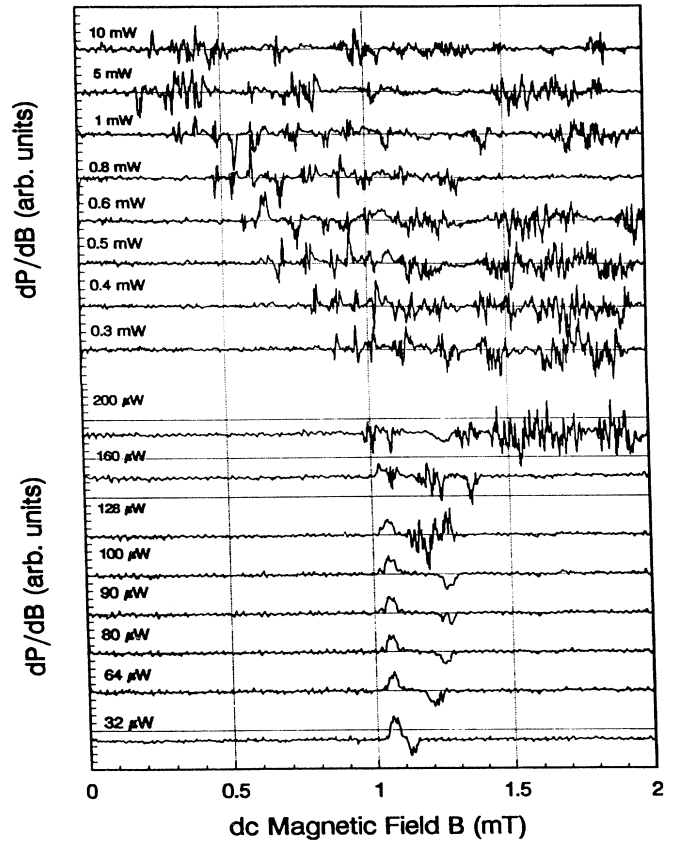


FIG. 6. The first type of line series measured for several microwave power levels ranging from  $16 \mu\text{W}$  to 10 mW. The sample was measured in the experimental configuration shown in the inset of Fig. 2.

above  $8 \mu\text{W}$ , whereas the next lines are obtained for lower power levels. The microwave power dependence for the first line is shown in more detail in Fig. 6, where the microwave power is varied from  $16 \mu\text{W}$  to 10 mW. The up-going peak of the line remains unchanged up to  $128 \mu\text{W}$ ; thereafter it moves to lower field values.

Figure 7 shows the second type of microwave absorption line series measured at different levels of microwave

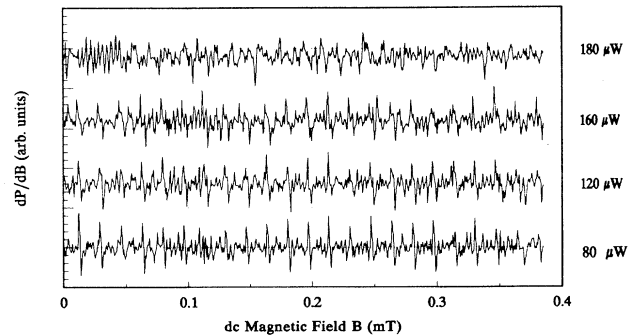


FIG. 7. The series of lines measured for several different microwave powers at 4.2 K. The sample was measured for the experimental configuration shown in the inset of Fig. 3.

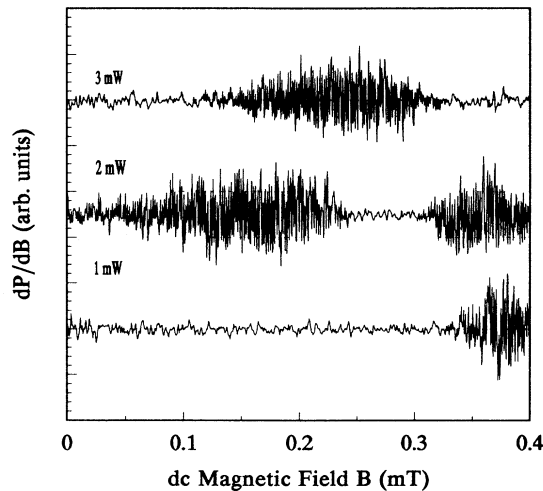


FIG. 8. Series of lines with a modulated amplitude recorded as a function of the input power. The sample was measured using the experimental configuration shown in the inset of Fig. 2.

power. The sample was measured in the configuration shown in the inset in Fig. 3. The lines appear for microwave power exceeding  $64 \mu\text{W}$  and their amplitudes increase with power. Above  $100 \mu\text{W}$  they split and, for microwave power larger than  $180 \mu\text{W}$ , the line separation ( $\delta B$ ) cannot be distinguished.

The third type of line series show higher power threshold than the first two series. In addition, the amplitude of these lines is not constant, but is modulated and more than one group of lines is observed. Figure 8 shows this kind of line series recorded for three different levels of microwave power ranging from 1 to 3 mW. The dc field location of the lines depends on the microwave power, and the lines shift and/or disappear with increasing power.

#### IV. JUNCTION MODEL

The microstructure of melt-textured YBCO is relatively well known (Ref. 17) and seems to be suitable to elucidate the origin of microwave absorption. It consists of platelets stacked along the  $c$  axis and connected through grain boundaries. Each platelet is segregated into domains by twin boundaries. In our samples all the grains are assumed to be oriented along a common  $c$  axis which is normal to the sample surface cut along the  $a$ - $b$  plane. The twin boundaries, aligned along  $\langle 110 \rangle$  directions, extend through the grain-boundary area. Since no rotation of the  $a$  or  $b$  axis was observed across the grain boundary it suggests that the platelets originated from the same nucleation center.<sup>19</sup> In that case the  $a$  ( $b$ ) axis orientation is common for the whole sample. The thickness of each grain is about  $10 \mu\text{m}$ , which is small compared to the length and width of the grains. The distance between the twin planes is in the range of 0.1 to 0.2  $\mu\text{m}$  depending upon the sample fabrication process.

This kind of grain structure can be described by a

brick-wall model.<sup>20</sup> This model is depicted in Fig. 9, and even though low-angle grain boundaries are not shown it captures all the essential features of the observed microstructure.<sup>21</sup> Each brick represents a local anisotropic superconductor which can be described by the London equation. A dc external magnetic field  $B$  is applied parallel to the  $a$ - $b$  planes and a rf magnetic field is applied along the  $c$  axis. We assume that  $B$  is smaller than the lower critical field  $B_{c1}$ . Thus screening currents induced in the sample flow on its surface within the effective penetration depth  $\lambda$  in the grains and  $\lambda_J$  on the edge of grain boundaries. The dashed lines indicate the profile of currents flowing in the grains and the grain boundaries. On each side of the grain boundary the field extends to a distance  $\lambda$ . The single arrows indicate induced dc currents whereas double arrows represent rf currents.

In this experiment the sample is small relative to the size of the microwave cavity; thus we can assume that the rf field is uniform around the sample and that the induced microwave current flowing across the junctions is in phase. It allows us, for modeling purposes, to isolate a single junction with the adjacent grains. In Fig. 9(b) the cross section of a single Josephson junction is shown, in isolation from the whole "brick-wall model." In this figure the rf field is parallel to the  $c$  axis and the dc field is parallel to the  $a$ - $b$  plane. The single and double arrows

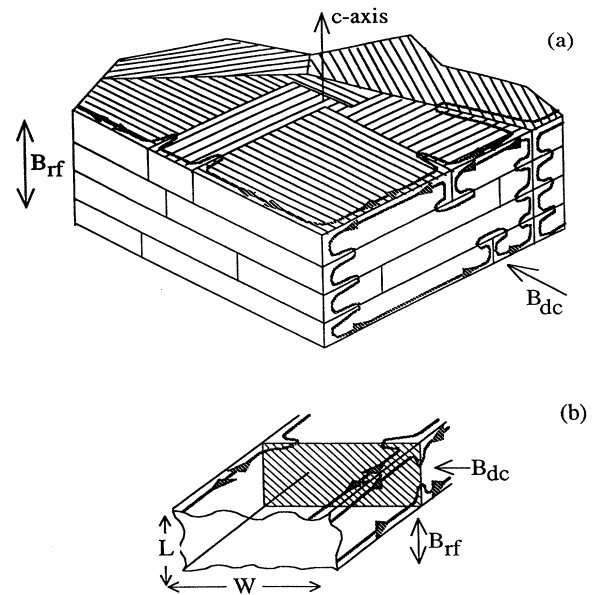


FIG. 9. (a) The brick-wall model for melt-textured samples. The thickness of the grain boundaries is not shown as it is very small in comparison with the junction dimensions. The thick solid lines are the profiles of the current penetration depths into the grains and the grain boundaries. Double arrows represent rf currents. The screening currents due to the presence of the dc magnetic field are marked by single arrows. (b) A single junction isolated from the brick-wall model. Two grains of width  $W$  and length  $L$  are coupled by a grain boundary. The dc magnetic field is parallel to the  $a$ - $b$  plane and the rf magnetic field is parallel to the  $c$  axis.

have the same meaning as in Fig. 9(a). Each superconducting grain has a width  $W$  and height  $L$  which are much larger than the effective penetration depth  $\lambda$ .

The Josephson penetration depth  $\lambda_J$  is used as a scale in the description of Josephson junctions. A junction with length  $L$  smaller than the Josephson penetration depth  $\lambda_J$  is called a short junction, where the magnetic field is always uniform. For this type of junction the magnetic field produced by the currents flowing through the junction is negligible in comparison to the externally applied field. In the case of a large junction, the length  $L$  of the junction is longer than  $\lambda_J$  and a self-field effect cannot be neglected. The field distribution inside the long junction is not uniform anymore.

A previous microwave study of the melt-textured material<sup>22</sup> showed the presence of both intra- and intergrain Josephson-coupled weak links. Therefore we expect to find a whole variety of superconductor-insulator-superconductor (SIS) and superconductor-normal-metal-superconductor (SNS) junctions with different strength and uniformity of coupling. For the purpose of interpretation of the experimental data, we will discuss both short and long as well as uniform and nonuniform SIS and SNS junctions.

It is well known that for small SIS junctions, i.e., with  $L/\lambda_J \ll 1$  and  $J_c$  a constant over the whole area of the junction, the critical current can be expressed as a function of magnetic field by

$$I_c(B) = I_0 \left| \frac{\sin(\pi B/\Delta B)}{\pi B/\Delta B} \right|. \quad (1)$$

Here  $I_0$  is the value of  $I_c$  at zero magnetic field, and  $\Delta B$  is the spacing between the minima of  $I_c$ .

For a uniform SIS junction with strong coupling, no analytic expression for a critical current is available. To find the spatial phase dependence we will follow the Owen and Scalapino approach.<sup>23</sup>  $I_c(B)$  can be found by solving  $\partial^2 \varphi / \partial x^2 = (1/\lambda_J) \sin \varphi$ , which describes the phase  $\varphi$  in the junction. This equation can be transformed into a standard elliptic integral form with standard Jacobian elliptic functions as solutions. Using a boundary condition obtained from the magnetic-field continuity along the junction edges, the critical current as a function of magnetic field can be found. Figure 10(a) shows numerical calculations of  $I_c(B)$  for  $L/\lambda_J$  equal to 4.

In superconductor-weak superconductor-superconductor (SS'S) or proximity SNS microbridgelike junctions, with the effective span  $d$  and  $L$  of the bridge about 3.5 and 4.4 times larger than the coherence length  $\xi$  in the superconducting banks, respectively,<sup>24</sup> the mechanism that controls the critical current is quite different from that in SIS junctions. For this particular case, Abrikosov vortices are formed in the bridge and their motion controls the critical currents. In all other cases, the critical current dependence on the magnetic field can be calculated according to the equation (Ref. 24)

$$I_c(B) = I_0 \frac{[(n+1) - B/\Delta B](B/\Delta B - n)}{B/\Delta B}. \quad (2)$$

Here  $B/\Delta B$  describes the number of vortices in the junc-

tion and is set between  $n$  and  $n+1$  ( $n < B/\Delta B < n+1$ ). Figure 10(b) shows the critical current  $I_c$  normalized to  $I_0$  as a function of  $B/\Delta B$  calculated from Eq. (2).

Junctions with uniform coupling or constant  $J_c$  should have the first minimum of the  $I_c(B)$  function at  $B/\Delta B = 1$ . However, we did not observe any series of absorption lines that would begin at this point. Instead, the first absorption line was obtained for the value of  $B/\Delta B$  in the range of 0.5 to 0.6. This indicates that the junctions in the melt-textured bulk have nonuniformity of both shape and coupling. The critical current versus magnetic field is described by a different function than that of uniform junctions. We will follow the model of a nonuniform SIS junction proposed by Barone and Paterno<sup>25</sup> by assuming that the coupling is stronger at the two ends of the junction than in the middle. The critical current of such a junction is described by the formula

$$J_c(x) = J_0 \frac{\cosh(\alpha x)}{\cosh(\alpha L/2)} = \frac{\cosh(2\chi x/L)}{\cosh(\chi)}. \quad (3)$$

The parameter  $\alpha$  gives a measure of the peak-to-valley ratio in the profile of the  $J_c(x)$  distribution, while  $\chi$  is equal to  $\alpha L/2$ . For a given  $\chi$ , the critical current as a function of applied magnetic field will have the shape

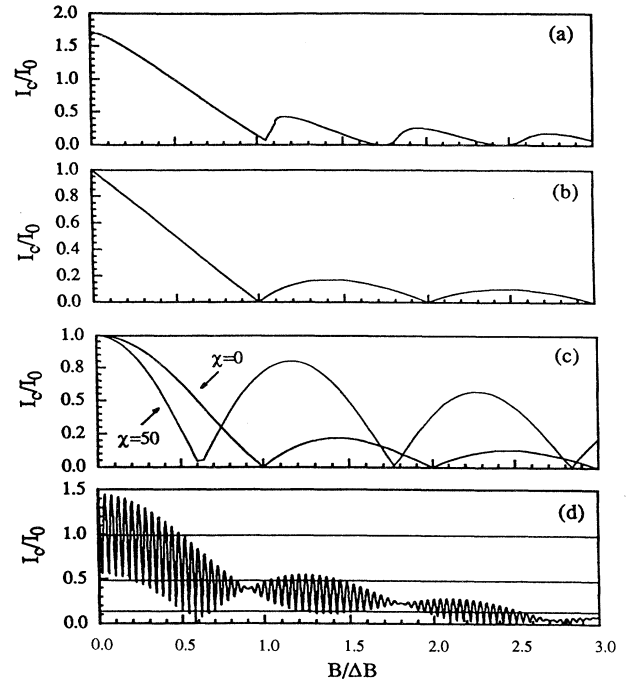


FIG. 10. Normalized critical current  $I_c/I_0$  versus normalized dc magnetic field  $B/\Delta B$  calculated for the following. (a) A uniform SIS junction with strong coupling. The value of  $L/\lambda_J$  was chosen to be equal to 4. (b) SS'S or proximity SNS microbridge junctions. Equation (2) was used for calculation. (c) Nonuniform junction. Equation (4) was used with two different values of  $\chi$  parameter: 0 and 50. (d) Nonuniform junction modeled as a network of two subjunctions. Equation (5) was used for the calculations with spacing  $\Delta B_{J1}$ ,  $\Delta B_{J2}$ , and  $\Delta B_L$  equal to 0.9, 3.0, and 0.04 mT, respectively.

$$I_c(B, \chi) = I_0 \frac{\chi^2}{\chi^2 + (\pi B / \Delta B)^2} \left| \frac{\pi B / \Delta B \sin(\pi B / \Delta B)}{\chi \tanh(\chi)} + \cos \left[ \pi \frac{B}{\Delta B} \right] \right|. \quad (4)$$

For the extreme case when  $\chi \rightarrow 0$  Eq. (4) is reduced to Eq. (1), which gives the first zero point,  $I_c(B) = 0$ , at one value of  $\Delta B$ . For the other extreme value of  $\chi \rightarrow \infty$ , we found that the first zero point has the limit at  $\Delta B/2$ . Thus by changing  $\chi$  we can obtain the first zero point of  $I_c(B)$  at any value of  $B/\Delta B$  between 0.5 and 1. Figure 10(c) shows two plots of  $I_c(B, \chi)$  calculated for  $\chi = 0$  and 50.

A nonuniform junction can be modeled as a network of many subjunctions. Each subjunction represents an area with stronger coupling. Subjunctions can represent microshorts in a single junction.<sup>26</sup> For simplicity we assume that the main junction consists only of two subjunctions. Each subjunction is characterized by its own critical current,  $I_{c1}$  and  $I_{c2}$ . The geometrical dimensions of the subjunctions determine the spacing between the minima of the  $I_c(B)$  function as  $\Delta B_{J1}$  and  $\Delta B_{J2}$ , respectively. Furthermore, again for simplicity we assume that the coupling in the area which separates two subjunctions is equal to zero. This structure resembles a superconducting quantum interference device (SQUID) loop with two junctions. In the presence of a magnetic field there will be a current loop flowing through these two subjunctions and circulating around that area. The magnetic flux which can be accommodated in this zero-coupling area can be parametrized by  $\Delta B_L$ , which corresponds to one quantum of the flux in this area. Since we are dealing with flux quantization in a microstructure, loop inductance and self-induced flux can be neglected. Thus the critical current which can flow through these subjunction systems is related to the applied magnetic field as follows:<sup>27</sup>

$$I_c(B) = \left\{ \left[ I_{c1} \left[ \frac{B}{\Delta B_{J1}} \right] - I_{c2} \left[ \frac{B}{\Delta B_{J2}} \right] \right]^2 + 4I_{c1} \left[ \frac{B}{\Delta B_{J1}} \right] I_{c2} \left[ \frac{B}{\Delta B_{J2}} \right] \times \cos^2 \left[ \pi \frac{B}{\Delta B_L} \right] \right\}^{1/2}. \quad (5)$$

If the two subjunctions have equal critical current then

$$I_c(B) = 2I_{cJ} \left[ \frac{B}{\Delta B_J} \right] \left| \cos \left[ \pi \frac{B}{\Delta B_L} \right] \right|. \quad (6)$$

Here the subscripts  $J$  and  $L$  stand for the subjunction and loop, respectively. Figure 10(d) shows the plot of Eq. (5) with  $\Delta B_{J1}$ ,  $\Delta B_{J2}$ , and  $\Delta B_L$  equal to 0.9, 3.0, and 0.04 mT, respectively.

## V. MICROWAVE ABSORPTION IN THE JUNCTIONS

Microwave absorption appears when the induced microwave current exceeds the critical current of the junction

suppressed by the applied magnetic field. To describe the electromagnetic junction behavior we will use the classical approach of McCumber<sup>28</sup> and Stewart<sup>29</sup> using the *small-capacitance* resistively shunted junction model. We will use the following nonlinear differential equation to find the supercurrent flowing through the junction:

$$\frac{I_{rf}}{I_\omega} e^{i\tau} = \frac{I_c(B)}{I_\omega} \sin\varphi + \frac{d\varphi}{d\tau} + \frac{I_c(B)}{I_\omega} \left[ \frac{\omega}{\omega_J} \right]^2 \frac{d^2\varphi}{d(\tau)^2}. \quad (7)$$

This equation is modified to dimensionless form by normalization to a microwave leakage current  $I_\omega = V_J/R_J$ , where  $V_J = \hbar\omega/2e$  and  $R_J$  represent the junction voltage and subgap resistance. In Eq. (7)  $\tau = \omega t$  where  $\omega$  is the angular microwave frequency,  $I_c$  is the critical current of the junction, and  $\omega_J = \sqrt{2eI_c/\hbar C}$  is the junction plasma frequency, where  $C$  denotes the junction capacitance.

A junction can be characterized now by three parameters:  $I_c$ ,  $I_\omega$ , and  $\omega_J$ . The leakage current is related to the junction barrier quality. The right-hand side of Eq. (7) represents three components of the whole current flowing through the junction: the Josephson tunneling current, the quasiparticle current, and the displacement current.

In a general form, Eq. (7), which is a nonlinear equation, can only be solved numerically. However, for small microwave power or large  $I_c$ -to- $I_{rf}$  ratio this equation can be linearized using the approximation  $I_s = I_c\varphi$  to obtain

$$I_{rf} e^{i\tau} = I_s(\tau) + \frac{I_\omega}{I_c} \frac{dI_s(\tau)}{d\tau} + \left[ \frac{\omega}{\omega_J} \right]^2 \frac{d^2I_s(\tau)}{d\tau^2}. \quad (8)$$

This equation has a phasor solution of the supercurrent  $I_{s0}$ , which is given by

$$I_{s0} = \frac{I_{rf}}{1 - (\omega/\omega_J) + i(I_\omega/I_c)}. \quad (9)$$

Dividing each side by  $I_c$  we obtain

$$\frac{I_{s0}}{I_c} = I_{rf} \left[ \frac{1}{I_c [1 + (\omega/\omega_J)^2] + iI_\omega} \right]. \quad (10)$$

By letting  $I_c$  go to zero we find that

$$\lim_{I_c \rightarrow 0} \left| \frac{I_{s0}}{I_c} \right| \rightarrow \left| \frac{I_{rf}}{I_\omega} \right|. \quad (11)$$

This result shows that when  $I_{rf}/I_\omega < 1$  the Josephson tunneling current will never exceed the critical current of the junction, even for infinitely small critical current. This is a case when the linear approximation works quite well. However, the linear approximation is not valid for the whole range of  $I_c$  when  $I_{rf}/I_\omega > 1$ , because for  $I_c \rightarrow 0$  at some particular value of  $I_c$ , which we call  $I_c^{abs}$ , the supercurrent  $I_s$  exceeds  $I_c$ . When  $I_c$  approaches  $I_c^{abs}$  the first large absorption takes place. It indicates that when  $I_c < I_c^{abs}$  Eq. (7) cannot be linearized. In the general case it can be shown that for  $I_c$  larger than  $I_\omega \sqrt{(I_{rf}/I_\omega)^2 - 1}$  the linear approach is correct. Therefore there are two cases of microwave absorption in junctions: linear when

$I_{rf} < I_\omega$  or  $I_c > I_\omega \sqrt{(I_{rf}/I_\omega)^2 - 1}$  and nonlinear when  $I_{rf} > I_\omega$  and  $I_c < I_\omega \sqrt{(I_{rf}/I_\omega)^2 - 1}$ . For the first case the power loss can be calculated from Eq. (10) by using the relation  $P = \frac{1}{2} I_n I_n^* R_J$ . Here  $I_n$  and  $I_n^*$  are both normal currents which are equal to  $i(I_\omega/I_c)I_{s0}$  and its complex conjugate, respectively. For this case the microwave power loss per unit time in the junction can be described by the formula

$$P(B) = \frac{\frac{1}{2} I_{rf}^2 R_J}{[I_c(B)/I_\omega]^2 [1 - (\omega/\omega_J)^2] + 1}. \quad (12)$$

When the microwave frequency  $\omega$  approaches the plasmon frequency  $\omega_J$  resonant absorption can occur. However, usually at practically used frequencies the term  $\omega/\omega_J$  is small and can be neglected. This case is equivalent to the linear, resistively shunted junction model for which the displacement current in Eq. (9) is neglected. Thus the microwave absorption becomes

$$P(B) = \frac{\frac{1}{2} I_{rf}^2 R_J}{[I_c(B)/I_\omega]^2 + 1}. \quad (13)$$

Figure 11 shows the absorption of microwave energy in the junction calculated using Eq. (13) with  $I_c(B)$  obtained from Eq. (1). A plot of the function  $P(B)$  is presented for two cases: (a) for a sample which contains junctions of the same geometrical size and (b) for a sample with junctions of a variable size characterized by some geometrical distribution.

For the nonlinear case when  $I_{rf} > I_\omega$ , there is no analytical solution for Eq. (7). However, the equation can be solved numerically. We neglect the displacement

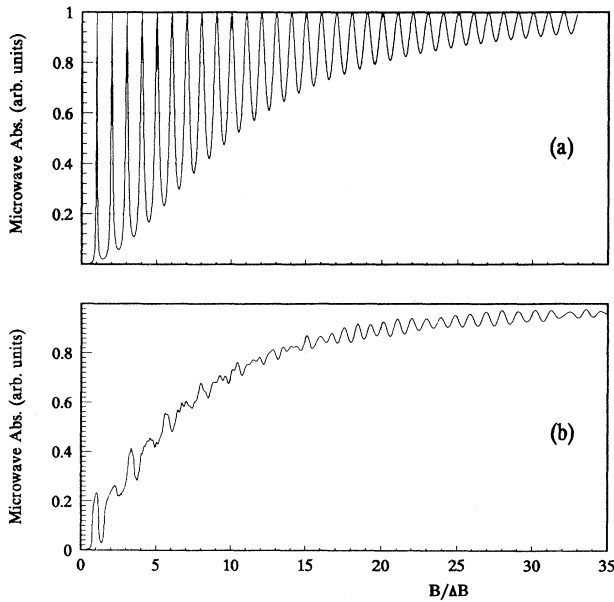


FIG. 11. Microwave absorption as a function of dc magnetic field  $B$  for a sample which contains junctions with the same size (a) and with some size distribution (b). Equations (1) and (13) were used for the calculation.

current and use  $I_{rf}/I_\omega$  and  $I_c(B)/I_\omega$  as two parameters for the numerical solution  $\varphi(\tau, I_{rf}/I_\omega, I_c(B)/I_\omega)$ . Differentiating  $\varphi$  numerically with respect to time ( $\Delta\varphi/\Delta\tau$ ) and using the Josephson voltage relation, we find the junction power loss as

$$P(B) = \frac{1}{2} I_{rf}^2 R_J \left[ \left( \frac{I_\omega}{I_{rf}} \right)^2 \left( \frac{\Delta\varphi}{\Delta\tau} \right)^2 \right]. \quad (14)$$

In Figure 12 an example of microwave power absorption versus junction critical current is shown for the  $I_{rf}/I_\omega$  ratio equal to 8. A sharp change in absorption occurs for the  $I_c/I_\omega$  ratio of 7 and is denoted as  $I_c^{abs}/I_\omega$ . The solutions  $\varphi(\tau)$  of Eq. (7) give the correlation between this sharp change in absorption and a sudden  $2\pi$  phase change during the period of microwave radiation.<sup>30</sup> The phase  $\varphi$  swings to a larger extent during one period in order to increase the Josephson voltage across the junction. This will increase the normal current to keep the total current in balance. This can be described as one fluxon oscillating in the junction. The dashed line in Fig. 12 represents the numerical derivative  $dP/dI_c$  versus  $I_c$  calculated from Eq. (14). In addition to the sharp peak at  $I_c/I_\omega$  equal to 7, another broader peak at a smaller value of  $I_c/I_\omega$  is clearly seen. This peak is related to another  $2\pi$  phase change. At this point two fluxons are oscillating in the junction. This second  $2\pi$  phase change causes smaller absorption than the first one, which results in a broader absorption peak. A detailed analysis of this dynamical flux quantization in the junction will be published elsewhere.

From the set of numerical solutions of Eq. (7) obtained by neglecting the displacement current, we can find the critical current ( $I_c^{abs}$ ) in the parameter space ( $I_{rf}/I_\omega, I_c/I_\omega$ ) at which a sharp absorption change occurs. The result of this calculation is presented in Fig. 13 with open circles. We find that for  $I_{rf}/I_\omega > 3$  we can use the approximation  $I_c^{abs} = I_{rf} - I_\omega$ . This indicates that whenever  $I_c(B) < I_c^{abs}$  junction phase slipping occurs and fluxons

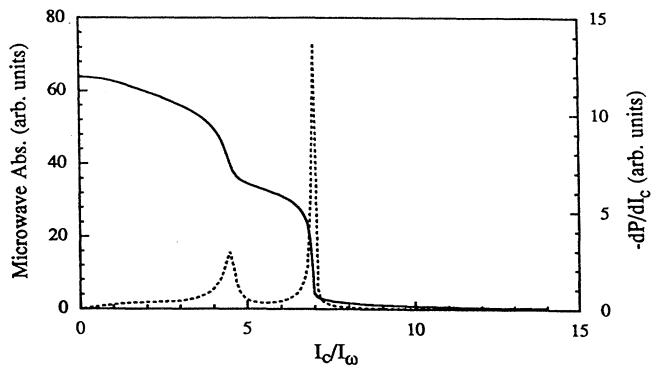


FIG. 12. Microwave absorption versus junction critical current for  $I_{rf}/I_\omega$  ratio equal to 8. A sharp rise of the microwave absorption is clearly seen around  $I_c/I_\omega = 7$ . The second broader rise of the absorption takes place at a smaller value of  $I_c/I_\omega$ . The dashed line represents the numerical derivative  $dP/dI_c$  versus  $I_c$ . The calculations were done using Eq. (14).

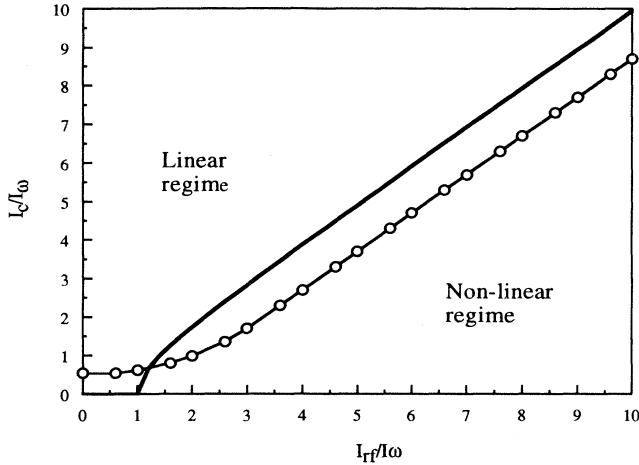


FIG. 13. A plot of  $I_c^{\text{abs}}/I_\omega$  versus the ratio of  $I_{\text{rf}}$  and  $I_\omega$ . The linear and nonlinear regimes of the absorption are shown.

start to oscillate in the junction. This results in the absorption of a large amount of microwave energy. Therefore, we can write the following expression which locates the onset of a large absorption for  $I_{\text{rf}}/I_\omega > 3$ :

$$P(B) = (\frac{1}{2}I_{\text{rf}}^2 R_J) \Theta(I_{\text{rf}} - I_\omega - I_c(B)). \quad (15)$$

Here  $\Theta$  is a step function.

In Fig. 13 the solid line is a plot of the function  $I_c/I_\omega = \sqrt{(I_{\text{rf}}/I_\omega)^2 - 1}$  which is the boundary line between the linear and nonlinear regimes of the absorption. From this figure we can also see that for low microwave power, when  $I_{\text{rf}}/I_\omega < 1$ , the absorption is in the linear regime and  $I_c^{\text{abs}}$  does not depend on  $I_{\text{rf}}$ . For this case, Eq. (13) can be used. For the nonlinear regime (when  $I_{\text{rf}}/I_\omega > 1$ ) numerical solutions are needed. However, for the case when  $I_{\text{rf}}/I_\omega > 3$ , Eq. (15) can be used as an approximation for locating the absorption peak.

In our measurements we have recorded the first derivative of the power loss  $P$  with respect to the magnetic field  $B$ . The first derivative of Eq. (15) is given by

$$\frac{dP}{dB} = -(\frac{1}{2}I_{\text{rf}}^2 R_J) \frac{dI_c}{dB} \delta(I_{\text{rf}} - I_\omega - I_c(B)). \quad (16)$$

The  $\delta$  function represents a sharp peak whenever  $I_c(B) = I_{\text{rf}} - I_\omega$ . We can see that when the derivative  $dI_c/dB$  is negative the peak is up-going; consequently, when  $dI_c/dB$  is positive the peak is down-going.

## VI. DISCUSSION

In Sec. IV we showed that the  $I_c(B)$  function for an extreme case of nonuniformity is equivalent to the  $I_c(B)$  of two or more subjunctions with a SQUID-like loop. Thus a real nonuniform single-plane-defect junction can be modeled as several subjunctions separated by weakly coupled areas. The effective Josephson penetration depth  $\lambda_J$  depends on the applied magnetic field. When the magnetic field is weak, only those subjunctions which are close to the edge of the plane defect are affected by the

field penetration. Higher field results in a larger number of subjunctions involved in the absorption and a chain of SQUID-like loops can be created. In this case the interference pattern becomes more complex [for example, see Fig. 10(d)].

If the  $I_c(B)$  function is known, the fields  $B_p$  at which the absorption lines appear can be calculated, for a given  $I_{\text{rf}}$ , using the nonlinear RSJ model introduced in Sec. V. Each value of the field  $B_p$  has to satisfy the equation

$$I_c(B) = I_c^{\text{abs}} \left[ \frac{I_{\text{rf}}}{I_\omega} \right] \approx I_{\text{rf}} - I_\omega.$$

We can neglect  $I_\omega$  when it is small compared to  $I_{\text{rf}}$ . The procedure described above can be reversed, namely, the  $I_c(B)$  function can be found from measured  $B_p$  values. By measuring  $dP/dB$  versus magnetic field ( $B$ ) at various levels of microwave power ( $W$ ) and knowing that  $I_{\text{rf}}$  is proportional to the square root of the microwave power, we can plot  $\sqrt{W}$  versus  $B_p$ , which is directly related to  $I_c(B)$ . The experimental data from Figs. 5 and 6 can be used to obtain a normalized  $\sqrt{W}$  function that characterizes the investigated junctions (Fig. 14). The straight line shown in this figure is very similar to both a strongly coupled SIS junction [Fig. 10(a)] and a SNS junction [Fig. 10(b)]. Since the straight line intersects the  $B$  axis at about 1.7 mT, it corresponds to a junction area  $S$  of about  $1 \mu\text{m}^2$ . For low fields only one subjunction is involved in the absorption and it remains in the Meissner state until the external field reaches 1.15 mT. This value can be considered as the lower critical field  $B_{c1J}$  of the subjunction and it includes the demagnetization effect. Above  $B_{c1J}$ , the flux penetrates through the first subjunction located near an edge of a plane defect and the field is screened out by the next subjunction located further inside the plane defect. This interrupts the single-

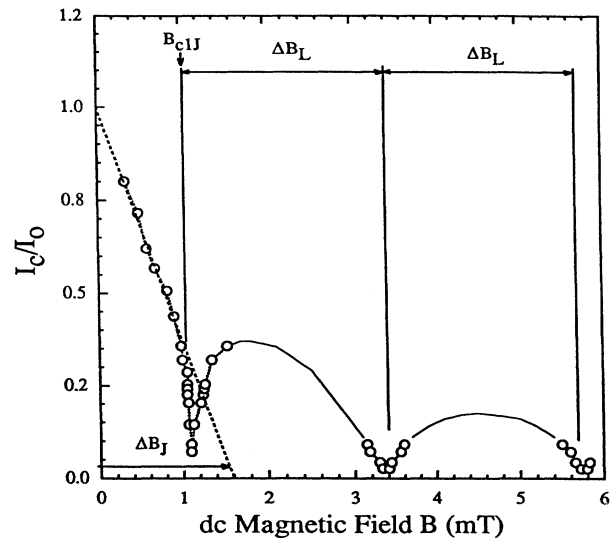


FIG. 14. Normalized critical current  $I_c/I_0$  versus dc magnetic field obtained from experimental data presented in Fig. 5 and 6. The solid line is a guide for the eyes. Straight line indicates Meissner state of the junction till 1.15 mT.

junction-type operation, and creates a SQUID-like loop interference effect of the two junctions. At that moment, the loop contains more than one flux quantum  $\Phi_0$  and the critical current of the system is different from zero. This explains the threshold for the appearance of the first absorption line. These two subjunctions seem to have nearly the same critical current, because the second and the third lines appear at very low power. From the above discussion we can conclude that the interference pattern presented in Fig. 14 consists of two parts: one corresponding to a single subjunction and the second corresponding to a SQUID-like loop. The line spacing for the junction ( $\Delta B_J$ ) and loop ( $\Delta B_L$ ) in Fig. 14 have the same meaning as in Eq. (5). An estimated value of  $\Delta B_J$  of each subjunction is about 1.7 mT. Since the separation between the first and the second or the second and third lines is 2.3 mT, the value of  $\Delta B_L$  is equal to 2.3 mT. The loop area, which is determined by the size of the weakly coupled region between the two subjunctions, can be calculated from  $\Delta B_L$  and is equal to  $1.4 \mu\text{m}^2$ .

The type of junction can be determined by the temperature dependence of the critical current. The analysis of such a temperature dependence, shown in Figs. 15(a) and 15(b), was obtained using the experimental data shown in Fig. 4. The line spacing is larger than 2.3 mT, because the measurements were done at an angle of  $50^\circ$  between the dc field and the [110] direction. For calculation purposes  $\Delta B$  was scaled to the minimum value using the  $1/\cos\Theta$  function (see Fig. 2). The subjunction area inter-

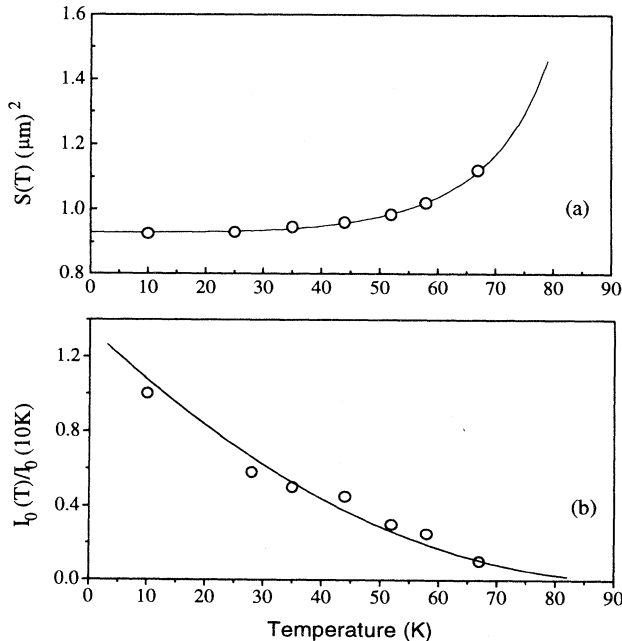


FIG. 15. Dependence of the effective area  $S$  of the junction on temperature (a). Solid line represents the simulation for the dependence of two-fluid-model penetration depth  $\lambda$  on temperature. Critical current  $I_0$  at zero magnetic field shown as a function of the temperature (b). Solid line represents the simulation of  $I_0(T)$  dependence for a SNS-type junction. For calculations, the experimental data from Fig. 4 were used.

cepted by the dc magnetic field is a function of temperature and if we neglect the barrier thickness it can be expressed as  $S(T) = \Phi_0 / \Delta B(T) = 2\lambda(T)L$ . Both  $\lambda$  and  $L$  have the same meaning as in Fig. 9. We can express the critical current as a function  $F$  of the  $SB_{1,2}$  product, where  $B_1$  and  $B_2$  are the dc magnetic-field values which correspond to the up-going and down-going peaks (see Fig. 4), respectively, in the following form:

$$\frac{I_c^{\text{abs}}}{I_0(T)} = F(S(T)B_1) = F(S(T)B_2). \quad (17)$$

The up-going and down-going peaks at  $B_1$  and  $B_2$  fields are related to  $I_c(SB_1)$  and  $I_c(SB_2)$  with a negative and a positive slope, respectively. In order to calculate the  $S(T)$  function we need to know the  $F(SB)$  function. We will use  $I_c(B)$  from Eq. (4), which seems to be a good approximation.

The  $S(T)$  data set presented in Fig. 15(a) is obtained numerically, using Eq. (17) and  $B_1$  and  $B_2$  values from Fig. 4. Using  $S(T)$  we can calculate the zero-field critical current  $I_0$  at different temperatures; which will be, however, scaled by an unknown proportionality constant between  $I_{rf}$  and  $\sqrt{W}$ . To eliminate this constant we can normalize  $I_0(T)$  to  $I_0$  at 10 K, thus obtaining the expression

$$\frac{I_0(T)}{I_0(10)} = \frac{F(S(10)B_1(10))}{F(S(T)B_1(T))}. \quad (18)$$

The results of this calculation is shown in Fig. 15(b) with open circles. The solid line represents the simulated temperature dependence of  $I_0$  for a typical SNS junction<sup>31</sup> which is scaled as  $(1 - T/T_c)^2$ . The very good agreement obtained between the data points and the fitting indicates that the subjunctions in the plane defects are of the SNS type.

Another important issue of these highly nonuniform SNS-type junctions is their location in the sample. Measurements of  $R_s$  in a dc magnetic field reveal the presence of both intra- and intergrain weak links in melt-textured YBCO (Ref. 14). The results presented in this paper provide more detailed information about the nature and the location of the weak links. In the literature, the results of flux quantization measurements are interpreted in terms of both single-junction absorption and loop theory. Blazey *et al.*<sup>12</sup> used a single-junction absorption approach and reported that the line spacing  $\Delta B$  is related to the cross section  $S$  of the  $\langle 110 \rangle$ -oriented twin boundaries. The area  $S$  was of the order of  $100 \mu\text{m}^2$  and was in agreement with other reports. The single-junction interpretation was also used by Kish, Tyagi, and Krafft<sup>15</sup> where lines due to both the dc and rf flux quantization in weak links were reported. Vichery, Beeuney, and Lejal *et al.*<sup>32</sup> interpreted their results in terms of a ringlike contour of area  $750 \mu\text{m}^2$  containing several weak links with a very small effective area.

From the angular dependence of the spacing between the lines, the location of plane defects and their symmetry can be analyzed. As shown earlier, the minimum of the line spacing  $\Delta B$  occurs when the dc magnetic field is parallel to the  $\langle 110 \rangle$  direction in the melt-textured sam-

ple. Since we have found that there are two sets of lines with angular dependencies shifted by  $90^\circ$  (see Fig. 2) the orthogonal symmetry of the plane defects which are related to this microwave absorption can be deduced. It is obvious that the best candidates for these plane defects are twin boundaries in the  $\{110\}$  plane which have such a  $90^\circ$  symmetry. However the twin boundaries cannot cause any flux quantization due to the fact that their separation, which varies from 0.1 to 0.2  $\mu\text{m}$ , is smaller than  $2\lambda$ . Thus the twin boundaries will cause only an increase of the London penetration depth  $\lambda$  to a larger effective value<sup>33</sup> and will have an influence on the surface resistance measurements, but should not be detected by field-modulated microwave-absorption measurements.

To find another candidate for the plane defects, we need to analyze the  $a$ - $b$  plane microstructure. The formation of twins in YBCO takes place during the phase transformation from tetragonal to orthorhombic. In the orthorhombic phase, the  $b$  lattice elongates and the  $a$  lattice contracts compared with the tetragonal phase, thus resulting in  $[110]$  twinning. The planes  $(110)$  and  $(\bar{1}10)$  are equivalent and both  $(110)$  and  $(\bar{1}10)$  types of twins can be formed in one grain. An interface between two orthogonal sets of twins consists of an alternation of the twin boundaries. Such an interface is sometimes called a complex twin boundary and is believed to have different properties than those of regular twin boundaries.<sup>34</sup> The complex twin boundaries seem to be responsible for the line series discussed above, because their separation is much larger than  $2\lambda$  and the complexity of oxygen distribution in the interface can produce the required nonuniformity of coupling.

An important aspect of the presented results is the number of plane defects involved in the microwave absorption represented by each line. A question might arise whether the lines shown in Fig. 4 can be related to the absorption only in one single junction or in several junctions of the same size. The measurements of one line in a small dc field scan showed that the lines have a substructure consisting of many narrow sublines. Figure 16(a) shows a narrow-range scan of the dc field for the first line of the series whose substructure is shown for different levels of microwave power. We have already attributed the presence of this line to a single subjunction in the complex twin boundary in the  $(110)$  plane. The overlap of the up-going and down-going peaks of the sublines in the 16  $\mu\text{W}$  spectrum gives very strong evidence for the existence of these subjunctions with a size distribution. The substructure indicates that these lines represent the microwave absorption in several subjunctions similar in size and loops from several different plane defects. Figure 16(b) shows a simulated absorption, assuming that the geometrical sizes of the junctions have a discrete distribution. The lines presented in this figure were simulated for 30 subjunctions with a discrete log-normal distribution of the area. For simplicity, we used the  $I_c(B)$  function from Eq. (1). The main features of the experimental results were simulated quite well. It is unclear, however, why the subline structure is equally, rather than randomly spaced. An instrumental effect was excluded. However, we can speculate that the increase of the subline spacing

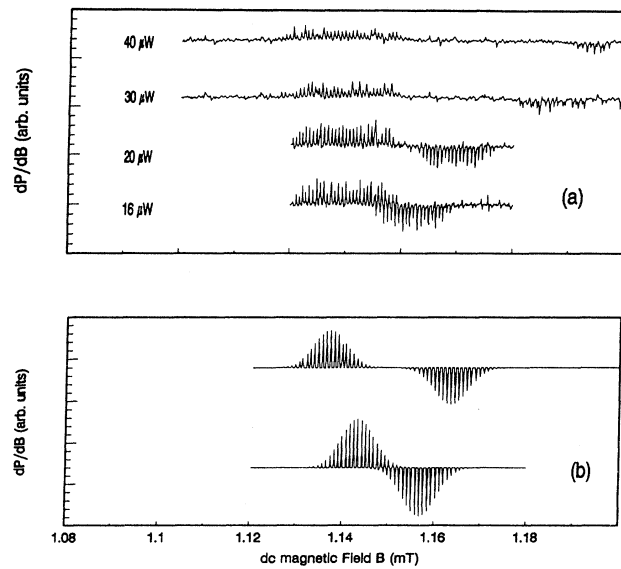


FIG. 16. The substructure of the first line from the first type of series (a). The absorption line was measured for four different power levels ranging from 16 to 40  $\mu\text{W}$ . (b) Simulation of the microwave absorption with the assumption that geometrical sizes of the junctions have a discrete distribution.

by 1.5  $\mu\text{T}$  corresponds to the decrease of the loop length by 10–11  $\text{\AA}$ . This is close to the lattice constant of the unit cell in the  $c$ -axis direction. It is consistent with the idea that the smallest possible change of the loop size in the complex twin boundary is equal to the length of the cell. This is based on the fact that in a complex twin boundary the size of an oxygen deficiency region can be changed only by the discrete length of one unit cell.<sup>35</sup>

The second and third types of line series (Fig. 1) were measured in the experimental configuration with  $B_{\text{rf}}$  parallel to the  $a$  ( $b$ ) axis. The angular (Fig. 3) and power (Fig. 7) dependence measurements showed that the lines can be attributed to the boundaries between the platelets. These boundaries can be modeled as a highly nonuniform junction. The line spacing for the series is very small, equal to 0.016 mT. The lines appear at a very low field and originate from a SQUID-like loop with at least two subjunctions. The line spacing is equivalent to 140  $\mu\text{m}^2$ . The subjunctions in platelet boundaries are much weaker than the subjunctions in complex twin boundaries.

From Fig. 7 (type-2 series) we can analyze the influence of rf power on  $\Delta B$  and on the separation ( $\delta B$ ) of the up- and down-going peaks. Both the  $\Delta B$  and  $\delta B$  values change with increasing power but above 160  $\mu\text{W}$ , a new series of lines emerge and the whole spectrum looks random, thus making the tracing of the peaks very difficult.

As the power increases further, additional equally spaced line series emerge, which can be seen in Fig. 8. Now the amplitude of the new line series is modulated. This is the type-3 [Fig. 1(c)] spectrum. The lines originate from SQUID-like loops, but this time each subjunction has a different critical current.  $I_c(B)$  for such a system schematically in Fig. 10(d). In this figure we show also

straight horizontal lines which represent the  $I_{rf}$  current at different power levels. The intersections of these lines with the  $I_c(B)$  function give the series of points which determine the positions of the amplitude-modulated line series shown in Fig. 8. The location and expansion of the intersected portion of the  $I_c(B)$  function depend on the rf power level. This can explain the shift or disappearance of whole groups of amplitude-modulated line series when the microwave power is changed. We have measured the angular dependence of  $\Delta B_L$  of these lines and we have found that it follows the  $1/\cos\varphi$  dependence. The  $\Delta B_L$  minimum value is equal to  $6\ \mu\text{T}$ .

In the case of a very weakly coupled junction, or when a very high microwave power is applied, there is no net current flowing through the junction and therefore the nonlinear RSJ model shown above is not valid anymore. The microwave magnetic-vortex-motion model should be used instead, for example. In this case the behavior of the lines as a function of rf power is very difficult. In the vortex-motion model, the lines in the series can be split, due to the applied rf power, by more than half the periodic spacing and still be recognized. According to the RSJ model the line splitting will never exceed half of the line spacing. When the split lines are in proximity to each other, they merge into a noiselike spectrum.

## VII. CONCLUSIONS

We have studied flux quantization in weak links in melt-textured  $\text{YBa}_2\text{Cu}_3\text{O}_{7-x}$  bulk using a modulated-microwave-absorption technique. We have used the nonlinear RSJ model combined with the special shape of an  $I_c(B)$  function as a framework for the interpretation of our experimental results. This model was used to deter-

mine the criteria for linear and nonlinear absorption in the junction to appear.

This study allowed us to identify the location and type of weak-link Josephson junctions and to determine the symmetry of the plane defects in which flux quantization takes place. These results, along with the microstructure data, indicate that intragrain complex twin boundaries and intergrain platelet boundaries are responsible for the microwave absorption in melt-textured YBCO.

Additionally, our experimental determination of the  $I_c(B)$  function and  $B_{c1J}$  field for SNS-type junctions, located most likely in the complex twin boundary, demonstrates the applicability of modulated-field microwave-absorption measurements to junction characterization. These results show that microwave-absorption measurements are useful for characterization of Josephson junctions not only in a melt-textured material but also in thin films; however, further experimental and theoretical effort is necessary to fully utilize the potential of this technique.

## ACKNOWLEDGMENTS

We are grateful to V. Selvamanickam and K. Salama for providing the samples for these studies. It is a pleasure to acknowledge stimulating discussions with Jürgen Halbritter. We also wish to express our thanks to J. H. Miller, Jr. and N. Tralshawala for critical reading of the manuscript and to M. F. Davis for his technical assistance. This work was supported by the State of Texas via Texas Center for Superconductivity at University of Houston and Texas Higher Education Coordinating Board (ARP grant).

<sup>1</sup>N. Klein, H. Choloupka, G. Müller, S. Orbach, H. Piel, B. Roas, L. Schultz, U. Klein, and M. Peiniger, *J. Appl. Phys.* **67**, 1 (1990).

<sup>2</sup>D. L. Rubin, K. Green, J. Gruschus, J. Kirchgessner, D. Moffat, H. Padamsee, J. Sears, Q. S. Shu, L. F. Schneemayer, and J. V. Waszczak, *Phys. Rev. B* **38**, 6538 (1988).

<sup>3</sup>S. Shridhar, D. H. Wu, and W. Kennedy, *Phys. Rev. Lett.* **63**, 1873 (1989).

<sup>4</sup>R. Durny, A. Dulcic, R. H. Crepeau, and J. H. Freed, *Physica C* **171**, 401 (1990).

<sup>5</sup>C. Kessler, B. Nebendahl, A. Dulcic, Th. Wolf, and M. Mehring, *Physica C* **192**, 79 (1992).

<sup>6</sup>M. Warden, M. Stalder, G. Stefanicki, A. M. Portis, and F. Waldner, *J. Appl. Phys.* **64**, 5800 (1988).

<sup>7</sup>K. W. Blazey, A. M. Portis, and F. H. Holtzberg, *Physica C* **157**, 16 (1989).

<sup>8</sup>A. Dulcic, R. H. Crepeau, and J. H. Freed, *Physica C* **160**, 223 (1989).

<sup>9</sup>K. W. Blazey, A. M. Portis, K. A. Müller, J. G. Bednorz, and F. Holtzberg, *Physica C* **153–155**, 56 (1988).

<sup>10</sup>W. K. Blazey, in *Earlier and Recent Aspects and Superconductivity*, edited by J. G. Bednorz and K. A. Müller, Springer Series in Solid State Sciences Vol. 90 (Springer, Berlin, 1990), pp. 236–277.

<sup>11</sup>M. Warden, L. Baselgia, D. Berlowitz, P. Erhart, B. Senning, M. Stalder, G. Stefanicki, A. M. Portis, and F. Waldner, in *24th AMPERE Congress, Poznań, 1988*, edited by J. Sankowski (Elsevier, New York, 1989), pp. 727–736.

<sup>12</sup>K. W. Blazey, A. M. Portis, K. A. Müller, and F. H. Holtzberg, *Europhys. Lett.* **6**, 457 (1988).

<sup>13</sup>J. E. Drumheller, Z. Trybula, and J. Stankowski, *Phys. Rev. B* **41**, 4743 (1990).

<sup>14</sup>J. Wosik, L. M. Xie, R. Chau, A. Samaan, J. C. Wolfe, V. Selvamanickam, and K. Salama, *Phys. Rev. B* **47**, 8968 (1993).

<sup>15</sup>T. K. Xia and D. Stroud, *Phys. Rev. B* **39**, 4792 (1989); K. Kish, S. Tyagi, and C. Krafft, *ibid.* **44**, 225 (1991).

<sup>16</sup>A. H. Silver and J. E. Zimmerman, *Phys. Rev.* **157**, 317 (1967).

<sup>17</sup>K. Salama, V. Selvamanickam, L. Gao, and K. Sun, *Appl. Phys. Lett.* **54**, 2352 (1989); V. Selvamanickam and K. Salama, in *High-Temperature Superconductors: Fundamental Properties and Novel Material Processing*, edited by D. K. Christen, J. Narayan, and L. F. Schneemeyer, MRS Symposia Proceedings No. 169 (Materials Research Society, Pittsburgh, 1990), p. 279.

<sup>18</sup>J. Wosik, R. A. Kranenburg, J. C. Wolfe, V. Selvamanickam and K. Salama, *J. Appl. Phys.* **69**, 874 (1991).

<sup>19</sup>K. B. Alexander, A. Goyal, D. M. Kroeger, V. Selvamanickam, and K. Salama, *Phys. Rev. B* **45**, 5622 (1992).

- <sup>20</sup>A. P. Malozemoff, in *High Temperature Superconducting Compounds II*, edited by S. H. Whang *et al.* (TMS Publications, Warrendale, PA, 1990), p. 3.
- <sup>21</sup>D. Shi, M. M. Fang, J. Akujieze, M. Xu, J. G. Chen, and C. Segre, *Appl. Phys. Lett.* **57**, 2606 (1990).
- <sup>22</sup>J. Wosik, L. M. Xie, J. Halbritter, R. Chau, A. Samaan, J. C. Wolfe, V. Selvamanickam, and K. Salama, *IEEE Trans. Appl. Supercond.* **3**, 1432 (1993).
- <sup>23</sup>C. S. Owen, and D. J. Scalapino, *Phys. Rev.* **164**, 538 (1967).
- <sup>24</sup>K. K. Likharev, *Rev. Mod. Phys.* **51**, 102 (1979).
- <sup>25</sup>A. Barone and G. Paterno, *Physics and Application of Josephson Effect* (Wiley, New York, 1982).
- <sup>26</sup>J. Halbritter, *Phys. Rev. B* **48**, 9735 (1993).
- <sup>27</sup>T. Van Duzer and C. W. Turner, *Principle of Superconductive Devices and Circuits* (Elsevier, New York, 1981).
- <sup>28</sup>D. E. McCumber, *J. Appl. Phys.* **39**, 3113 (1968).
- <sup>29</sup>W. C. Stewart, *Appl. Phys. Lett.* **12**, 237 (1968).
- <sup>30</sup>L. M. Xie, J. Wosik, and J. C. Wolfe (unpublished).
- <sup>31</sup>P. G. de Gennes, *Rev. Mod. Phys.* **36**, 225 (1964).
- <sup>32</sup>H. Vichery, F. Beeuneu, and P. Lejal, *Physica C* **159**, 823 (1989).
- <sup>33</sup>H. Deutscher, in *Earlier and Recent Aspects and Superconductivity* (Ref. 10), p. 182.
- <sup>34</sup>A. Rosova, C. Boulesteix, and I. Vavra, *Physica C* **214**, 247 (1993); Y. Zhu, M. Suenaga, and J. Taftø, *Philos. Mag. A* **67**, 1057 (1993).
- <sup>35</sup>S. Semenovskaya and G. A. Khachatryan, *Philos. Mag. Lett.* **66**, 105 (1992).